WENO Schemes for Mixed-Element Unstructured Meshes

V. A. Titarev*, P. Tsoutsanis and D. Drikakis

*Fluid Mechanics and Computational Sciences Group, Aerospace Sciences
Department, Cranfield University, Cranfield, MK43 0AL, UK.*

Abstract. The paper extends weighted essentially non-oscillatory (WENO) schemes to two-dimensional quadrilateral and mixed-element unstructured meshes. The key element of the proposed methods is a reconstruction procedure suitable for arbitrarily-shaped cells. The resulting schemes achieve the designed uniformly high-order of accuracy and compute discontinuous solutions without spurious oscillations at interfaces between cells of two different types.

1   Introduction

Weighted essentially non-oscillatory (WENO) schemes [1,6,10,11,14,19] represent a popular class of high-order methods for hyperbolic conservation laws. These methods combine very high-order of spatial accuracy when the solution is smooth and at the same time do not produce spurious oscillations near sharp gradients or across discontinuities. Originally, the schemes were developed and applied on structured Cartesian meshes. Unstructured meshes are more suitable for practical applications with complicated geometries. Therefore, WENO schemes have been extended to two-dimensional triangular meshes [6,10] and three-dimensional tetrahedral meshes [3,4,25]. Accurate results were obtained for a number of difficult test cases thus showing the potential of the methods.

The aim of the present work is to develop finite-volume WENO methods both for two-dimensional quadrilateral and mixed-element unstructured meshes, comprising quadrilateral and triangular elements. The motivation is twofold. Firstly, numerical modelling of viscous flows often requires the use of mixed-element meshes in which quadrilateral

---

*Corresponding author. *Email addresses:* `v.a.titarev@cranfield.ac.uk`, `titarev@mail.ru` (V. A. Titarev), `takis10@hotmail.com` (P. Tsoutsanis), `d.drikakis@cranfield.ac.uk` (D. Drikakis)

cells are typically used inside the boundary layers where the rest of the computational domain is discretised by triangular cells. Therefore, numerical methods should be able to use unstructured meshes consisting of elements of different types and not purely triangular ones. Secondly, the use of quadrilateral meshes may lead to better computational efficiency due to the use of fewer elements and larger time step.

The paper is organised as follows. In Section 2 the general framework of finite-volume WENO schemes on mixed-element meshes is outlined. In Section 3 a detailed explanation of both linear and nonlinear reconstruction for a scalar variable is provided. This reconstruction can be viewed as an extension of the WENO methodology proposed in [3, 4]. The application of the developed technique to the compressible Euler equations is discussed in Section 4. Section 5 presents numerical results, which demonstrate the very high-order accuracy of the resulting methods, their essentially non-oscillatory properties as well as illustrate the influence of the mesh quality on the accuracy of the calculations. Conclusions are drawn in Section 6.

2   The numerical framework

Consider a two-dimensional hyperbolic system of the form

$$\frac{\partial}{\partial t}\mathbf{U}+\frac{\partial}{\partial x}\mathbf{F}(\mathbf{U})+\frac{\partial}{\partial y}\mathbf{G}(\mathbf{U})=\mathbf{0},\tag{2.1}$$

where $\mathbf{U}$ is the vector of conserved variables; $\mathbf{F}$, $\mathbf{G}$ are flux vectors in the $x-$ and $y-$ coordinate directions, respectively. Suppose that the computational domain is discretised by conforming elements E_i of the area $|E_i|$, indexed by a unique mono-index i. Vertices $\mathbf{x}^{(l)}=(x^{(l)},y^{(l)})$ and sides of each element are indexed by $l=1,\cdots,L(i)$ with $\mathbf{x}^{(L(i)+1)}=\mathbf{x}^{(1)}$. The centre of the element has coordinates (x_i,y_i).

Integrating (2.1) over an element i in space, the following semi-discrete finite-volume method is obtained :

$$\frac{d}{dt}\bar{\mathbf{U}}_i+\frac{1}{|E_i|}\int_{\partial E_i}\mathbf{H}_n ds=\mathbf{0},\quad \mathbf{H}_n=n_x\mathbf{F}+n_y\mathbf{G},\tag{2.2}$$

where $\mathbf{n}=(n_x,n_y)$ is the outward unit normal vector of the cell E_i and $\bar{\mathbf{U}}_i(t)$ are the cell averages of the solution at time t. The integral over the boundary ∂E_i is split into the sum of integrals over each side l resulting in the following expression:

$$\frac{d}{dt}\bar{\mathbf{U}}_i=\mathbf{R}_i,\quad \mathbf{R}_i=-\frac{1}{|E_i|}\sum_{l=0}^{L(i)}\int_{\mathbf{x}^{(l)}}^{\mathbf{x}^{(l+1)}}\mathbf{H}_n ds=-\frac{1}{|E_i|}\sum_{l=0}^{L(i)}\mathbf{H}_{il}.\tag{2.3}$$

In the computational framework, the intercell flux $\mathbf{H}_{il}$ corresponding to the side l of the cell E_i is approximated by a suitable Gaussian numerical quadrature:

$$\mathbf{H}_{il}=\sum_{\beta}\mathbf{H}_n\left(\mathbf{U}(\mathbf{x}_\beta,t)\right)\omega_\beta|A_l|,\tag{2.4}$$

where the subscript β corresponds to different Gaussian integration points $\mathbf{x}_\beta$ and weights ω_β over the side A_l; $|A_l|$ is the length of the side. Evaluation of the numerical flux according to (2.4) requires the reconstruction of the point-wise values of the solution from cell averages. In order to avoid spurious oscillations, the reconstruction must be solution-adaptive [7]. Since at each Gaussian point there are two possible reconstructed values of $\mathbf{U}$ given by the reconstruction polynomials, from inside the cell E_i and from the neighboring cell $E_{i'}$, the resulting discontinuity has to be resolved by means of a certain monotone function of two vector arguments, called a Riemann solver.

The cell averages of the solution are advanced in time using the third-order TVD Runge-Kutta method [11] (the index i for simplicity is dropped):

$$\bar{\mathbf{U}}^{(n+1/3)} = \bar{\mathbf{U}}^n + \Delta t \mathbf{R}(\bar{\mathbf{U}}^n),$$
$$\bar{\mathbf{U}}^{(n+2/3)} = \frac{3}{4}\bar{\mathbf{U}}^n + \frac{1}{4}\bar{\mathbf{U}}^{(n+1/3)} + \frac{1}{4}\Delta t \mathbf{R}(\bar{\mathbf{U}}^{(n+1/3)}), \tag{2.5}$$
$$\bar{\mathbf{U}}^{n+1} = \frac{1}{3}\bar{\mathbf{U}}^n + \frac{2}{3}\bar{\mathbf{U}}^{(n+2/3)} + \frac{2}{3}\Delta t \mathbf{R}(\bar{\mathbf{U}}^{(n+2/3)}).$$

The time step Δt is selected according to the formula

$$\Delta t = K \min_i \Delta_i, \quad \Delta_i = \frac{h_i}{V_i}, \tag{2.6}$$

where V_i is an estimate of the maximum propagation speed in cell E_i, $K \le 1/2$ is the CFL number and h_i is the characteristic length of the element E_i. In general, for triangular elements, h_i is the diameter of the inscribed circle, whereas for quadrilateral elements h_i is taken to be the length of the smallest side of the element E_i.

The description of the semi-discrete scheme (2.3)-(2.5) is complete once a reconstruction procedure to calculate the point-wise values of the solution from cell averages is given. In the following sections details on the reconstruction procedure, used in the present work, are provided.

3 Scalar reconstruction procedure

In finite-volume methods, the advection scheme (2.3) advances in time cell-averaged values of the solution, whereas the flux calculation needs the point-wise values. These point-wise values have to be calculated from cell averages by means of a piecewise polynomial reconstruction procedure carried out for each computational cell (mesh element) E_i. In this section the arbitrary-order-accurate essentially weighted non-oscillatory reconstruction procedure on mixed-element unstructured meshes is described. It is sufficient to explain the idea for a scalar variable $u(x,y)$, which does not depend on time. To simplify notation, the global spatial index i is omitted and the local numbering of cells is introduced. The reconstruction problem can thus be reformulated as follows: for a target cell E_0 build a high-order polynomial $p(x,y)$ that has the same cell average as the

reconstructed function u on the target cell

$$\bar{u}_0 = \frac{1}{|E_0|} \int\limits_{E_0} p(x,y)\,dxdy. \tag{3.1}$$

The reconstruction procedure will use the cell average of $u(x,y)$ on the target cell E_0 as well as averages $\bar{u}_j$ from the reconstruction stencil formed by neighboring cells E_j, $j=1,2,\cdots,j_{\max}$.

   The rest of the Section is organised as follows. Firstly, the linear single-stencil reconstruction is described in detail, consisting of the stencil assembly procedure and the solution of the reconstruction equations. Then, the non-oscillatory version of the reconstruction for mixed-element meshes is presented, which includes the new selection procedure for direction stencils.

   It should be noted that although the present paper considers triangular ($L(i)=3$) and quadrilateral ($L(i)=4$) elements only, the developed algorithm extends directly to polygonal meshes.

3.1   Linear reconstruction

In general, the reconstruction can be carried out in the physical coordinates (x,y), taking special measures against mesh scaling effects. However, a more elegant and computationally convenient approach is to use the so-called reference coordinate system (ξ,η). For triangular (2D) and tetrahedral (3D) meshes this has been done in [3]. Here, this mapping meshes is extended to mixed-element. For a cell E_i the reference coordinate system is defined by a linear mapping from the physical coordinate system (x,y) given by the formula

$$\begin{pmatrix} x \\ y \end{pmatrix} = \begin{pmatrix} x^{(1)} \\ y^{(1)} \end{pmatrix} + J \begin{pmatrix} \xi \\ \eta \end{pmatrix}, \tag{3.2}$$

where the transformation Jacobian J is defined by

$$J = \begin{pmatrix} x^{(2)} - x^{(1)} & x^{(L(i))} - x^{(1)} \\ y^{(2)} - y^{(1)} & y^{(L(i))} - y^{(1)} \end{pmatrix}. \tag{3.3}$$

   For triangular elements this coincides with the mapping introduced in [3]. There are thus the direct and inverse mapping from $\boldsymbol{\xi}=(\xi,\eta)$ into $\boldsymbol{x}=(x,y)$, which are denoted as

$$\boldsymbol{x}=x(\boldsymbol{\xi}), \quad \boldsymbol{\xi}=\xi(\mathbf{x}). \tag{3.4}$$

Via the inverse mapping (3.4) the target element E_0 can be transformed to the element E_0' in the reference coordinate system. For the uniform (Cartesian) quadrilateral mesh the transformed element E_0' is just a unit square in the reference space (ξ,η). For general non-uniform meshes three of its four vertices of the transformed element will still be

from the unit square, although the element as a whole will no longer be a unit square. This is different from the case of triangles in which all triangular cells of the mesh are transformed into the unique reference triangle, see [3] for more details. Note that spatial average of $u(x,y)$ does not change during transformation:

$$\bar{u}_0 = \frac{1}{|E_0|} \int\limits_{E_0} u(x,y)\, dxdy \equiv \frac{1}{|E_0'|} \int\limits_{E_0'} u(\xi,\eta)\, d\xi d\eta.$$

For performing the reconstruction on the target element E_0, the so-called central reconstruction stencil $\mathcal{S}$ is formed, which consists of $(j_{max}+1)$ elements, including the target element E_0:

$$\mathcal{S} = \bigcup_{j=0}^{j_{max}} E_j,$$

where the local index j counts the elements in the stencil $\mathcal{S}$. The stencil is built up by recursively adding the direct side neighbours of the element E_0 and all of the elements added to the stencil so far, until the desired number j_{max} of stencil elements is reached. Note that if there are more neighbouring cells then required for the stencil construction, the closest ones are chosen, that is the ones which centres lie closer to the centre of the cell i. The inverse mapping (3.4) is then applied to all the elements E_j from the reconstruction stencil $\mathcal{S}$ and denote the transformed elements and stencil as E_j' and $\mathcal{S}'$, respectively:

$$\mathcal{S}' = \bigcup_{j=0}^{j_{max}} E_j'.$$

The reconstruction polynomial at the transformed cell E_0' is sought as an expansion over local polynomial basis functions $\phi_k(\xi,\eta)$:

$$p(\xi,\eta) = \sum_{k=0}^{K} a_k \phi_k(\xi,\eta) = \bar{u}_0 + \sum_{k=1}^{K} a_k \phi_k(\xi,\eta), \tag{3.5}$$

where a_k are degrees of freedom and the upper index in the summation of expansion K is related to the degree of the polynomial r by the expression $K = \frac{1}{2}(r+1)(r+2)-1$. The conservation condition (3.1) impose an important constraint on the basis functions: they must have zero mean value over the cell E_0'. On triangular meshes hierarchical orthogonal reconstruction basis functions defined on the reference triangle satisfy this requirement automatically [3]. Since quadrilateral cells are not necessarily transformed onto a unit square, basis functions ϕ_k need to be constructed in such a way that condition (3.1) is satisfied identically irrespective of values of degrees of freedom. In the present work they are defined as follows:

$$\phi_k \equiv \psi_k - \frac{1}{|E_0'|} \int\limits_{E_0'} \psi_k\, d\xi d\eta, \quad \{\psi_k\} = \xi,\, \eta,\, \xi^2,\, \xi\cdot\eta,\cdots, \quad k=1,2,\cdots,K. \tag{3.6}$$

To find the unknown degrees of freedom a_k it is required that for each cell E'_m from the stencil $\mathcal{S}'$ the cell average of the reconstruction polynomial $p(\xi,\eta)$ be equal to the cell average of the solution $\bar{u}_m$:

$$\int\limits_{E'_j} p(\xi,\eta)\,d\xi d\eta = |E'_j|\bar{u}_0 + \sum_{k=1}^{K}\int\limits_{E'_j} a_k\phi_k\,d\xi d\eta = |E'_j|u_j, \quad j=1,\cdots,j_{\max}.$$

Let A_{jk} be the cell averages of the basis function k over the cell j in the stencil

$$A_{jk} = \frac{1}{|E'_j|}\int\limits_{E'_j}\phi_k\,d\xi d\eta.$$

Also denote $b_j = (\bar{u}_j - \bar{u}_0)$. Then the equations for degrees of freedom a_k can ne rewritten in the matrix form as

$$\sum_{k=1}^{K} A_{jk}a_k = b_j, \quad j=1,2,\cdots,j_{\max}. \tag{3.7}$$

The two-dimensional integrals on the left-hand side of (3.7) are calculated using Gaussian quadratures of appropriate orders [15].

In general, in order to compute the degrees of freedom a_k the stencils should consist of at least K cells, different from the target cell E_0. However, the use of the minimum possible number of cells in the stencil $j_{\max} \equiv K$ results in a scheme which may become unstable on general meshes. It is therefore recommended to use more cells in the stencil then the minimal required number [2,3,12]. Usually the value $j_{\max} = 1.5 \cdot K$ is used.

Since $j_{\max} > K$, the matrix A_{jk} is rectangular and system (3.7) for the unknown degrees of freedom a_k is over-determined. The least-square approach usually used to solve (3.7) is well suited for the methods of up to 3rd order of accuracy. For higher-order polynomials it results in the linear system, the condition number of which is approximately the square of the condition number of matrix A. This may affect the accuracy for smooth problems and very fine meshes. An alternative to the least square method is the so-called singular value decomposition (SVD) approach [5], in which the rectangular matrix A of dimensions $K \cdot j_{\max}$ is directly decomposed into the product of three matrices

$$A = U \cdot D \cdot V^T,$$

where U is an $j_{\max} \times K$ column-orthogonal matrix, W an $K \times K$ diagonal matrix with non-negative elements (singular values) and V an orthogonal $K \times K$ matrix. The use of SVD results in a robust solution for the unknown degrees of freedom and also allows to estimate the condition number of the matrix A. Therefore, in the present work the SVD decomposition procedure is used throughout. The matrices U, W and V involved in the solution procedure are precomputed and stored for each element during the preprocessing stage of the calculation, thus increasing the computational efficiency of the method.

3.2   WENO reconstruction on mixed-element meshes

Details on existing types of WENO reconstructions for triangular cells can be found in [10, 25] and [3] as well as references therein. The reconstruction proposed of the present work is an extension and modification of [3] with regards to mixed-element meshes, consisting of both triangular and quadrilateral cells.The WENO reconstruction stencils is a union of several reconstruction stencils $\mathcal{S}_m$, $m=0,1,\cdots,m_s$. These comprise one central stencil and several one-sided, or sectorial, stencils. The use of multiple stencils allows the scheme to adapt itself to the discontinuities in the solution in the essentially non-oscillatory manner.
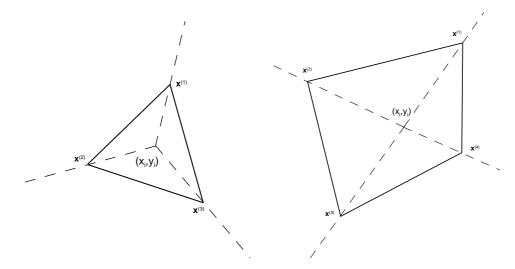

Figure 1: Sectors for the construction of direction stencils.

The sectorial stencils $\mathcal{S}_m$ in the physical coordinate system, are obtained by adding only those neighbouring cells, centres of whose centres lie inside the given sector. Each sector m in the present work is defined by two rays, which are formed by connecting the cell centre (x_i,y_i) and two vertices: $\mathbf{x}^{(m)}$ and $\mathbf{x}^{(m+1)}$, see Fig. 1 for a graphical illustration. The number of sectorial stencils is thus equal to the number of sides of the cell $m_s \equiv L(i)$ except near solid boundaries. The position of the centers of candidate neighbouring cells related to the spatial sector number m can be easily checked as follows. First define the transformation to the local coordinate system s

$$\begin{pmatrix} x \\ y \end{pmatrix} = \begin{pmatrix} x_i \\ y_i \end{pmatrix} + J \begin{pmatrix} \xi \\ \eta \end{pmatrix}, \quad J = \begin{pmatrix} x^{(m)} - x_i & x^{(m+1)} - x_i \\ y^{(m)} - y_i & y^{(m+1)} - y_i \end{pmatrix}, \tag{3.8}$$

so that the sector becomes $\xi \geq 0$, $\eta \geq 0$. Then apply (3.8) to the centre of the candidate cell and check if it lies inside the sector. Since the sectors constructed in such a way cover all possible directions, there is no need to use the so-called reverse sectors suggested in [12]. While assembling cells for each of the sectorial stencils, it is made sure that sectorial stencils do not overlap. Overall, our reconstruction procedure uses a significantly smaller

number of stencils compared to the original construction [3], where $m_s = 6$ is used for triangular elements.

The WENO reconstruction polynomial is now defined as a non-linear combination of reconstruction polynomials $p_m(\xi,\eta)$, obtained by using individual stencils $\mathcal{S}_m$:

$$p_{\text{weno}} = \sum_{m=0}^{m_s} \omega_m p_m(\xi,\eta). \tag{3.9}$$

Substitution of the form of the individual polynomial (3.5) corresponding to the stencil $\mathcal{S}_m$

$$p_m(\xi,\eta) = \sum_{k=0}^{K} a_k^{(m)} \phi_k(\xi,\eta) = \bar{u}_0 + \sum_{k=1}^{K} a_k^{(m)} \phi_k(\xi,\eta)$$

and the use of the condition $\sum_m \omega_m \equiv 1$ yields

$$p_{\text{weno}} = \sum_{m=0}^{m_s} \omega_m \left(\sum_{k=0}^{K} a_k^{(m)} \phi_k(\xi,\eta) \right) = \bar{u}_0 + \sum_{m=0}^{m_s} \omega_m \left(\sum_{k=1}^{K} a_k^{(m)} \phi_k(\xi,\eta) \right)$$

$$= \bar{u}_0 + \sum_{k=1}^{K} \left(\sum_{m=0}^{m_s} \omega_m a_k^{(m)} \right) \phi_k(\xi,\eta) \equiv \bar{u}_0 + \sum_{k=1}^{K} \tilde{a}_k \phi_k(\xi,\eta). \tag{3.10}$$

Here, $\tilde{a}_k$ are the new values of degrees of freedom, modified according to the WENO procedure. The nonlinear WENO weights ω_m are defined as [10, 11]

$$\omega_m = \frac{\gamma_m}{\sum\limits_{m=0}^{m_s} \gamma_m}, \quad \gamma_m = \frac{d_m}{(\varepsilon + IS_m)^p}, \tag{3.11}$$

where d_m are the so-called linear weights; IS_m are smoothness indicators; ε is a small number used to avoid division by zero; and finally p is an integer parameter, controlling how fast the non-linear weights decay for non-smooth stencils. Typically the following values are used: $\varepsilon = 10^{-6}$ and $p = 4$. Note that for some applications the choice of these two parameters may have a profound effect on the numerical solution, see, e.g., [18].

Our selection of linear weights d_m follows [3]. The central stencil is assigned a large linear weight $d_0 = 10^2, \cdots, 10^3$ whereas the sectorial stencils are assigned smaller weights $d_m = 1$. This selection of the weights is motivated by the fact that for smooth solutions the central stencil is usually the most accurate one. A similar concept was used in [12] in two spatial dimensions with equal weights assigned to all stencils.

The oscillation indicators IS_m of each stencil is a measurement of how smooth the solution is on this stencil. Due to the use of the reference coordinate system, scaling is already taken out of the problem and IS_m can be computed in a mesh-independent manner as

$$IS_m = \sum_{1 < |1 < \beta < r} \int_{E_0'} \left(D^\beta p_m(\xi,\eta) \right)^2 d\xi d\eta, \tag{3.12}$$

where β is a multi-index, r is the degree of the polynomial and D is the derivative operator; for example when $\beta=(1,2)$, then $|\beta|=3$ and

$$D^{\beta}p(\xi,\eta)=\frac{\partial^3 p(\xi,\eta)}{\partial\xi\partial\eta^2}.$$

It is easily seen that the smoothness indicators (3.12) are quadratic functions of degrees of freedom $a_k^{(m)}$ and thus the expression (3.12) can be rewritten as

$$IS_m=\sum_{p=1}^K a_p^{(m)}\left(\sum_{q=1}^K b_{pq}a_q^{(m)}\right), \tag{3.13}$$

where $B=\{b_{pq}\}$ is the so-called oscillation indicator matrix [3]. If the mesh consists of triangular elements only, then this matrix is universal and does not depend on the element. However, for quadrilateral elements B_{pq} will depend on the element because a general quadrilateral cell is not transformed to a unit square. The general form of B in three space dimensions can be found in [3]. For the two-dimensional case it is simplified into

$$b_{pq}=\sum_{1<|1<\beta<K|}\int_{E_0'}\left[D^{\beta}\phi_p(\xi,\eta)\right]\left[D^{\beta}\phi_q(\xi,\eta)\right]d\xi d\eta.$$

For example, for second-order schemes $r=1$ and

$$b_{pq}=\int_{E_0'}\left(\frac{\partial\phi_p}{\partial\xi}\frac{\partial\phi_q}{\partial\xi}+\frac{\partial\phi_p}{\partial\eta}\frac{\partial\phi_q}{\partial\eta}\right)d\xi d\eta.$$

The oscillation indicator matrix is precomputed and stored for each cell element at the beginning of the calculations.

3.3 Examples of stencils

Some examples of stencils construction are presented below. The stencils are first constructed in the physical coordinate system and then mapped to the reference coordinate system (ξ,η) using the linear transformation (3.2)-(3.3). Consider a quadrilateral cell i of a mixed-element mesh with direct neighbours of both types. Fig. 2 shows cells from all stencils used in the third-order WENO reconstruction in both the physical and reference coordinate systems. Highlighted is the central stencil. The cell i with the center coordinates $(0.5314,0.6383)$ is also marked. The central stencil is build up by adding neighbours in the physical space x,y irrespective of their shape. It is not entirely symmetric because the cells are added according to their distance from the center of the cell i in the physical coordinate system (x,y). This procedure minimizes the spatial size of the stencil thus making the reconstruction more compact. Fig. 3 shows each of the sectorial stencils, corresponding to four sides of the cell. Note that the stencils are completely disjoint. Fig. 4
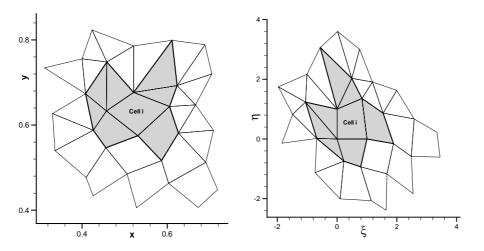
Figure 2: Central stencil in the physical (x,y) and reference (ξ,η) coordinate systems for the 3rd-order scheme.
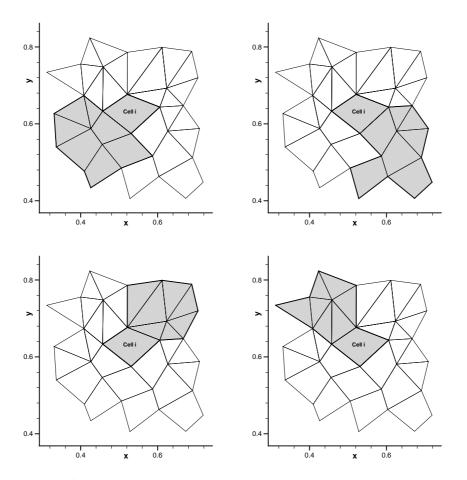
Figure 3: Sectorial stencils in the physical coordinate system for the 3rd-order scheme.
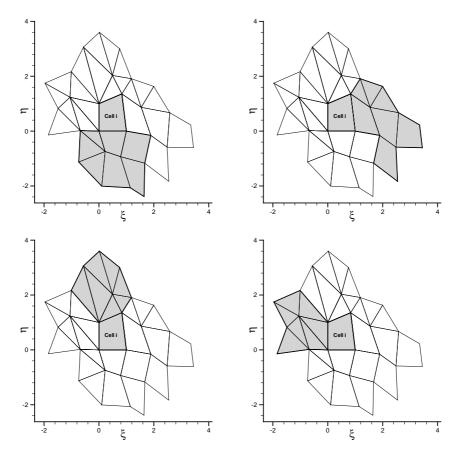
Figure 4: Sectorial stencils in the reference coordinate system for the 3rd-order scheme.

shows the same sectorial stencils but in the reference coordinate system. It is seen that the central cell *i* is transformed into the quadrilateral element three out of four vertices of which have the coordinates $(0,0)$, $(1,0)$ and $(0,1)$. Other cells, however, are not transformed into unit elements.

4   Application to the compressible Euler equations

Here the developed reconstruction technique is applied to the compressible Euler equations of gamma-law gas of the form (2.1) with:

$$\mathbf{U} = \begin{pmatrix} \rho \\ \rho u \\ \rho v \\ E \end{pmatrix}, \quad \mathbf{F}(\mathbf{U}) = \begin{pmatrix} \rho u \\ \rho u^2 + p \\ \rho uv \\ u(E+p) \end{pmatrix}, \quad \mathbf{G}(\mathbf{U}) = \begin{pmatrix} \rho v \\ \rho vu \\ \rho v^2 + p \\ v(E+p) \end{pmatrix},$$

$$p = (\gamma - 1)(E - (1/2)\rho(u^2 + v^2)),$$

(4.1)

where ρ, u, v, p and E are density, velocity components in the x and y coordinate directions, pressure and total energy, respectively; γ is the ratio of specific heats, with $\gamma = 1.4$ being used throughout.

4.1   Reconstruction in characteristic variables

Calculation of the numerical flux (2.4) through the side A_l of a cell E_i requires knowledge of point-wise values of the conserved vector **U** at the Gaussian points. However, the numerical method advances in time the cell averages of the conserved vector. Therefore, high-order approximations to the point-wise values of the conserved vector at each Gaussian point of a face need to be obtained by using a high-order non-oscillatory reconstruction procedure. This is done by using the WENO reconstruction procedure on mixed-element meshes, based on the reconstruction of a scalar function u, developed in the previous section and extended here to vector variables. The reconstruction produces the high-order polynomials $\mathbf{P}_i(\xi,\eta)$ defined in the reference coordinate system. For a system of equation the reconstruction procedure should be carried out in characteristic variables rather than conservative variables, otherwise spurious oscillations may be produced even for simple shock-tube problems. Our approach for extending the scalar reconstruction to the characteristic-based reconstruction is very similar to that of [4], although different in some respects, and thus only the main steps are outlined below.

Consider the cell E_i and the corresponding set of directional stencils in the local reference coordinate system $\{S'_m\}$, $m=0,1,\cdots,m_s$. First the vector degrees of freedom $\mathbf{A}_{ik}^{(m)}$ are calculated for each stencil by applying the linear scalar reconstruction procedure in a component-wise fashion. Then the average value $\mathbf{U}'_n$ is defined as the arithmetic average of the conserved vector $\mathbf{U}_i$ and the conserved vector $\mathbf{U}_{i'}$, corresponding to the computational cell adjacent to the side A_l of the current cell E_i. Furthermore, denote by $\boldsymbol{R}_l$ and $\boldsymbol{L}_l$ the matrices containing the right and left eigenvectors of the Jacobian matrix of the normal projection of the flux tensor $\mathbf{H}_n$, calculated at this average state. The characteristic projections of vector degrees of freedom of each stencil S_m, including the cell averaged value $\mathbf{U}_i$, are computed as

$$\mathbf{B}_{ikl}^{(m)} = \mathbf{L}_l \mathbf{A}_{ik}^{(m)}, \quad m=0,\cdots,m_s, \quad k=0,\cdots,K.$$

The scalar WENO reconstruction algorithm is now applied to each component of the projected degrees of freedom. The resulting modified degrees of freedom $\tilde{\mathbf{B}}_{ikl}^{(m)}$ are projected back to the conserved formulation to give the final WENO vector degrees of freedom:

$$\tilde{\mathbf{A}}_{ik}^{(m)} = \mathbf{L}_l \tilde{\mathbf{B}}_{ikl}^{(m)}, \quad m=0,\cdots,m_s, \quad k=0,\cdots,K.$$

The final WENO reconstruction polynomial for the side l is given by

$$\mathbf{P}_{il}(\xi,\eta) = \bar{\mathbf{U}}_i + \sum_{k=1}^{K} \tilde{\mathbf{A}}_{ikl} \phi_{ik}(\xi,\eta), \tag{4.2}$$

where ϕ_{ik} are basis functions for the element E_i. The reconstructed WENO values at Gaussian integration points (ξ_β,η_β) on side l are then given by $\mathbf{P}_{il}(\xi_\beta,\eta_\beta)$. Note that the values of the basis functions at Gaussian integration points can be calculated and stored during the pre-processing step, increasing the efficiency of the method.

An additional step in the reconstruction process was used in [4], which consists of selecting the least oscillatory of all possible WENO polynomials and then using for all faces. In our calculations, this stage of the reconstruction is skipped as it is found to be unnecessary.

4.2 Flux calculation

In general, the numerical flux in (2.3) is evaluated using a suitable Gaussian numerical quadrature:

$$
\mathbf{H}_{il} = \int_{x^{(l)}}^{x^{(l+1)}} \mathbf{H}\cdot\mathbf{n}\,ds = \sum_{\beta=1}^{N_\beta} \mathbf{H}_\beta k_\beta, \quad \mathbf{H}_\beta = n_x\mathbf{F}(\mathbf{U}_\beta)+n_y\mathbf{G}(\mathbf{U}_\beta), \quad \mathbf{U}_\beta = \mathbf{U}(x_\beta,y_\beta,t), \qquad (4.3)
$$

where the subscript β corresponds to different Gaussian integration points (x_β,y_β) and weights k_β along the element side.

Evaluation of the numerical flux (4.3) consists of several steps. Firstly, for each cell E_i and each component of the conserved vector $\mathbf{U}_i$ piece-wise polynomial reconstruction is carried out and reconstruction polynomials $\mathbf{P}_{il}$ are built up. Next, high-order accurate approximations $\mathbf{P}_{il}(\xi_\beta,\eta_\beta)$ to the values of the conserved vector at the Gaussian integration points along the element side are calculated. After the reconstruction is carried out at each Gaussian point β there are two values of the conserved vector $\mathbf{U}$. The first value $\mathbf{U}_\beta^-$ corresponds to the spatial limit to the cell boundary from inside the cell E_i and is given by the reconstruction polynomial $\mathbf{P}_{il}$. The second value $\mathbf{U}_\beta^+$ corresponds to the spatial limit from outside the element and is obtained by using the reconstruction polynomial of the neighboring element. The values $\mathbf{U}_\beta^\pm$ are called left and right boundary extrapolated values. In upwind Godunov-type methods the resulting discontinuity is resolved by replacing $\mathbf{H}_\beta$ by a certain monotone function $\hat{H}$ of $\mathbf{U}^\pm$ so that (4.3) can be rewritten as

$$
\mathbf{H}_{il} = \sum_{\beta=1}^{N_\beta} \hat{H}\left(\mathbf{U}_\beta^-,\mathbf{U}_\beta^+\right)k_\beta. \qquad (4.4)
$$

The function $\hat{H}$ is called the Riemann solver [7], or a building block of a high-order scheme. For a review of such building blocks for various hyperbolic systems see [13,21]. In this paper the HLL Riemann solver [9] is used. Using the concept of the rotational invariance [21], define the rotated conserved variables

$$
\hat{\mathbf{U}}_L = \mathbf{T}_j\mathbf{U}_\beta^-, \quad \hat{\mathbf{U}}_R = \mathbf{T}_j\mathbf{U}_\beta^+.
$$

The HLL flux is given by

$$\hat{\mathbf{F}}^{HLL} = \begin{cases} \hat{\mathbf{F}}_L, & \text{if} \quad 0 \leq S_L, \\ S_R \hat{\mathbf{F}}_L - S_L \hat{\mathbf{F}}_R + S_L S_R (\hat{\mathbf{U}}_R - \hat{\mathbf{U}}_L), & \text{if} \quad S_L \leq 0 \leq S_R, \\ \hat{\mathbf{F}}_R, & \text{if} \quad 0 \geq S_R, \end{cases} \tag{4.5}$$

where S_L, S_* and S_R are the wave speeds to be estimated. The pressure-velocity estimates from [21] are used in the present work.

5   Numerical results

In this section numerical results and convergence studies are presented for three test problems. The main aim of these studies is three fold. Firstly, it is shown that for smooth solutions our schemes achieve the designed order of accuracy on mixed-element meshes, including the cases with rapid changes in cell sizes and generally pure-quality highly distorted meshes. Secondly, it is demonstrated, that the schemes provide good results when used to compute discontinuous solutions on mixed-element meshes. In other words, the presence of the interface between quadrilateral and triangular parts of the mesh does not degrade the accuracy of the results. Finally, the methods are applied on mixed element meshes with boundary layers, in which the area near the solid wall region is meshed with quadrilateral cells and the rest of the domain is discretized with triangles. The objective is to show that the presence of a solid wall boundary does not destabilize the calculations.

Since the present paper is devoted to the construction of the advection schemes rather than the aspects of the unstructured mesh generation and its comparison with block-structured approaches, in all the test cases simple rectangular computational domains are used. The main emphasis is thus placed on the assessment of the performance of the schemes. For all results presented below a fixed Courant number $K = 0.4$ is chosen in the time selection procedure according to (2.6) as well as the same central linear weight $d_0 = 100$ in the WENO reconstruction (3.11). In other words, no adjustment of scheme parameters is used to suit a particular test problem.

For the convergence studies schemes with third- and fifth-order spatial reconstructions are selected, and are denoted as Linear-3 and Linear-5 for linear schemes and WENO-3 and WENO-5 for WENO schemes, respectively. Since the third-order accurate time evolution method (2.5) is used, the resulting methods are of only third order of formal accuracy. However, the Linear-5 and WENO-5 schemes are still referred to in the text as 'fifth'-order accurate methods. If one wishes to obtain uniformly fourth and higher order of accuracy both in time and space, an ADER-type time evolution approach is recommended [3, 4, 16, 20, 22, 23].

5.1   Two-dimensional vortex evolution problem

The Euler equations (4.1) are solved in the square domain $[-5:5]^2$ with periodic boundary conditions. The initial condition corresponds to a smooth two-dimensional vortex placed

at the origin of the $x-y$ plane and is defined as the following isentropic perturbation to the uniform flow of unit values of primitive variables [1]:

$$u = \frac{\varepsilon}{2\pi} e^{\frac{1-r^2}{2}}(-y), \quad v = \frac{\varepsilon}{2\pi} e^{\frac{1-r^2}{2}}(x), \quad w = 0,$$

$$T = \frac{(\gamma-1)\varepsilon^2}{8\gamma\pi^2} e^{1-r^2}, \quad \frac{p}{\rho^\gamma} = 1, \quad r^2 = x^2 + y^2,$$

(5.1)

where the vortex strength is $\varepsilon = 5$. The exact solution is a vortex movement in the $x-y$ plane with a constant velocity at $45°$ to the Cartesian mesh lines. The numerical solution is computed at the output time $t = 2$.
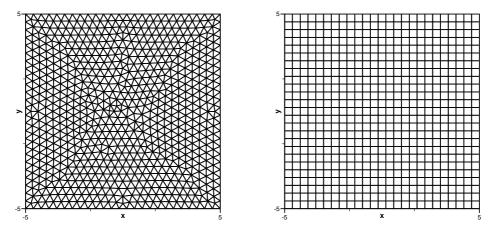

Figure 5: Uniform triangular (left) and quadrilateral (right) computational meshes used for the vortex evolution problem.

Each boundary (edge) of the considered square domain is discretised by N uniform cells and consider three types of meshes: triangular mesh, quadrilateral mesh and mixed-element mesh with both triangular and quadrilateral elements. Tables 1 and 2 show the results of both linear (central stencil) and WENO methods for the output time $t = 2$ on triangular and quadrilateral meshes, illustrated on Fig. 5 for $N = 25$. Numerical errors and convergence rates are measured in L_∞ and L_1 norm for cell averages of density. It is observed that the schemes operate close to the designed order of convergence for both mesh types. Moreover, WENO-5 scheme is significantly more accurate, than WENO-3; for the mesh with $N = 100$ the difference in accuracy is almost two orders of magnitude.

The results of Tables 1 and 2 also allow us to study the relative efficiency of different types of unstructured meshes. It is obvious that for a given number of boundary cells N the use of the triangular elements leads to the most accurate results. However, in practical applications the numerical error should be taken as a function of the computational time, which is in turn proportional to three parameters. The first one is the total number of spatial cells in the domain N_{tot}. The second one is the number of time steps N_t, required to reach the selected output time. Finally, the computational cost required to compute the

Table 1: Convergence study for the test problem (5.1) at output time $t=2$. Uniform quadrilateral meshes.

Scheme	N	L_∞ error	L_∞ order	L_1 error	L_1 order
Linear-3	25	5.07×10^{-2}		2.83×10^{-1}	
	50	9.80×10^{-3}	2.37	5.21×10^{-2}	2.44
	100	1.38×10^{-3}	2.83	7.48×10^{-3}	2.80
	200	1.82×10^{-4}	2.91	9.52×10^{-4}	2.97
WENO-3	25	5.83×10^{-2}		3.41×10^{-1}	
	50	1.03×10^{-2}	2.50	4.90×10^{-2}	2.80
	100	1.21×10^{-3}	3.09	6.71×10^{-3}	2.87
	200	1.59×10^{-4}	2.93	8.37×10^{-4}	3.00
Linear-5	25	2.83×10^{-2}		1.02×10^{-1}	
	50	1.36×10^{-3}	4.38	8.43×10^{-3}	3.60
	100	6.71×10^{-5}	4.34	3.62×10^{-4}	4.54
	200	2.56×10^{-6}	4.71	1.32×10^{-5}	4.77
WENO-5	25	2.56×10^{-2}		1.10×10^{-1}	
	50	1.39×10^{-3}	4.21	8.62×10^{-3}	3.67
	100	7.54×10^{-5}	4.20	3.99×10^{-4}	4.43
	200	3.01×10^{-6}	4.65	1.61×10^{-5}	4.64

Table 2: Convergence study for the test problem (5.1) at output time $t=2$. Uniform triangular meshes.

Scheme	N	L_∞ error	L_∞ order	L_1 error	L_1 order
Linear-3	25	1.86×10^{-2}		1.10×10^{-1}	
	50	3.66×10^{-3}	2.35	1.85×10^{-2}	2.57
	100	4.75×10^{-4}	2.94	2.46×10^{-3}	2.91
	200	5.92×10^{-5}	3.00	2.99×10^{-4}	3.04
WENO-3	25	1.81×10^{-2}		1.15×10^{-1}	
	50	3.69×10^{-3}	2.29	1.75×10^{-2}	2.72
	100	4.53×10^{-4}	3.03	2.33×10^{-3}	2.91
	200	5.59×10^{-5}	3.02	2.81×10^{-4}	3.05
Linear-5	25	6.39×10^{-3}		2.61×10^{-2}	
	50	2.50×10^{-4}	4.68	1.36×10^{-3}	4.26
	100	9.12×10^{-6}	4.77	4.54×10^{-5}	4.91
	200	2.97×10^{-7}	4.94	1.67×10^{-6}	4.77
WENO-5	25	5.58×10^{-3}		2.58×10^{-2}	
	50	2.38×10^{-4}	4.55	1.27×10^{-3}	4.35
	100	8.17×10^{-6}	4.86	4.26×10^{-5}	4.89
	200	2.91×10^{-7}	4.81	1.96×10^{-6}	4.44

numerical fluxes for one cell also plays its role. Table 5 summarizes first two parameters, N_{tot} and N_t. With regards to the third parameter, one has to take into account that the bulk of the cost is associated with the WENO reconstruction, which is in turn proportional to the number of stencils for the given cell shape. Therefore, one can assume that the

Table 3: Convergence study for the test problem (5.1) at output time $t=2$. Uniform mixed-element meshes.

Scheme	N	L_∞ error	L_∞ order	L_1 error	L_1 order
Linear-3	25	4.11×10^{-2}		2.12×10^{-1}	
	50	7.56×10^{-3}	2.44	3.60×10^{-2}	2.56
	100	1.05×10^{-3}	2.85	5.01×10^{-3}	2.85
	200	1.35×10^{-4}	2.96	6.40×10^{-4}	2.97
WENO-3	25	4.66×10^{-2}		2.22×10^{-1}	
	50	6.90×10^{-3}	2.76	3.53×10^{-2}	2.65
	100	9.49×10^{-4}	2.86	4.60×10^{-3}	2.94
	200	1.20×10^{-4}	2.98	5.72×10^{-4}	3.01
Linear-5	25	2.65×10^{-2}		7.60×10^{-2}	
	50	9.60×10^{-4}	4.78	4.50×10^{-3}	4.08
	100	4.29×10^{-5}	4.49	1.73×10^{-4}	4.70
	200	1.42×10^{-6}	4.91	5.79×10^{-6}	4.90
WENO-5	25	2.23×10^{-2}		6.91×10^{-2}	
	50	9.78×10^{-4}	4.51	4.34×10^{-3}	3.99
	100	4.73×10^{-5}	4.37	1.93×10^{-4}	4.49
	200	1.75×10^{-6}	4.75	7.07×10^{-6}	4.77

Table 4: Convergence study for the test problem (5.1) at output time $t=2$. Distorted mixed-element meshes.

Scheme	N	L_∞ error	L_∞ order	L_1 error	L_1 order
Linear-3	25	4.11×10^{-2}		2.12×10^{-1}	
	50	7.56×10^{-3}	2.44	3.60×10^{-2}	2.56
	100	1.05×10^{-3}	2.85	5.01×10^{-3}	2.85
	200	1.35×10^{-4}	2.96	6.40×10^{-4}	2.97
WENO-3	25	5.24×10^{-2}		2.38×10^{-1}	
	50	7.32×10^{-3}	2.84	3.73×10^{-2}	2.67
	100	1.11×10^{-3}	2.72	4.48×10^{-3}	3.06
	200	1.32×10^{-4}	3.07	5.46×10^{-4}	3.04
Linear-5	25	2.65×10^{-2}		7.60×10^{-2}	
	50	9.60×10^{-4}	4.78	4.50×10^{-3}	4.08
	100	4.29×10^{-5}	4.49	1.73×10^{-4}	4.70
	200	1.42×10^{-6}	4.91	5.79×10^{-6}	4.90
WENO-5	25	2.23×10^{-2}		6.90×10^{-2}	
	50	9.78×10^{-4}	4.51	4.34×10^{-3}	3.99
	100	4.73×10^{-5}	4.37	1.93×10^{-4}	4.49
	200	1.75×10^{-6}	4.75	7.07×10^{-6}	4.77

calculation of intercell fluxes for a quadrilateral cell is approximately $(5/4)=1.25$ times more expensive than for a triangular cell.

Table 5 shows that the quadrilateral elements are at least as efficient as the triangular ones. A graphical illustration of this is provided in Fig. 6, in which the L_0 error is plotted

Table 5: Summary of the total number of elements N_{tot} and the number of time steps N_t for meshes, used for the vortex evolution test problem (5.1).
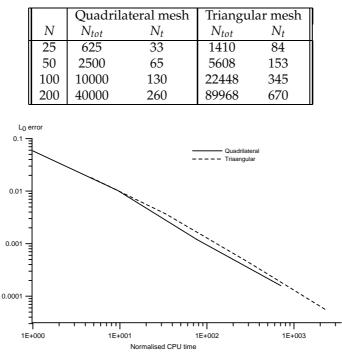
	Quadrilateral mesh		Triangular mesh	
N	N_{tot}	N_t	N_{tot}	N_t
25	625	33	1410	84
50	2500	65	5608	153
100	10000	130	22448	345
200	40000	260	89968	670

Figure 6: Error in L_0 norm as a function of the CPU time for the WENO3 method as applied to the vortex evolution problem.

against the CPU time it takes to run for a particular mesh; the values of CPU times are normalised by the time of the run on the coarsest 25×25 quadrilateral mesh. It is seen that indeed the quadrilateral mesh is slightly more computationally efficient for any given level of accuracy (numerical error).

The schemes have been tested on a sequence of mixed-element meshes, corresponding to $N = 25, 50, 100$ and 200. Each mesh in the sequence is constructed as follows: inside the computational domain $[-5:5]^2$. A quadrilateral subdomain is selected, defined by the vertices $(-3,0)$, $(3,0)$, $(1,3)$, $(-1.5,-3)$. Each of the sides of this subdomain is discretised into $N/2$ intervals and then is meshed with quadrilateral cells. The sides of the main computational domain are divided into N intervals as before, and the space between domain boundaries and the inner quadrilateral subdomain is meshed with triangles. Both the uniform meshes and perturbed (distorted) meshes are considered. The distorted mesh is obtained from the initial uniform mesh by randomly shifting vertex coordinates inside the domain. Fig. 7 shows both the uniform and perturbed mixed-element meshes for $N = 25$. As is seen, the perturbed mesh is significantly non-uniform with rather abrupt changes in cell areas and shapes. The poor quality of the perturbed mesh makes it ideal for testing the robustness of the numerical methods.
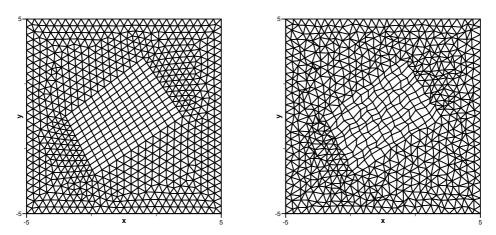
Figure 7: Uniform (left) and perturbed (right) mixed-element computational meshes with $N=25$ used for the vortex evolution problem.

The results of the calculations are given in Tables 3 and 4 for both third- and fifth-order schemes. The numerical convergence rate of the third-order methods are practical equal to the designed third order. For the fifth-order accurate versions of the scheme the numerically observed convergence rates are slightly below the fifth order. This may be due to the pure mesh quality and or insufficient mesh resolution. It is also seen that severe perturbations to the mesh results in only mild increase in the computational error for some of the mesh resolutions. It can therefore be concluded that the reduction of the numerical convergence rate at the interface between cells of two different types is very low and the schemes perform well for pure quality mixed-element meshes.

For the rest of the section only the results of the third-order scheme are shown as the most practical version of the method.

5.1.1 Two-dimensional explosion test problem

The solution of the so-called cylindrical explosion test problem [21] is calculated. The initial condition defined on $[-1\!:\!1]^2$ consists of two regions of constant but different values of gas parameters separated by a circle of radius 0.4:

$$(\rho,p)=\left\{\begin{array}{ll} (1.0,\,1.0), & r\leq 0.4, \\ (0.125,\,0.1), & r>0.4, \end{array}\right. \quad u=v=0, \quad r^2=x^2+y^2. \tag{5.2}$$

For this test problem the computational domain consists of a sector corresponding to $0\leq r\leq 1$ and the opening angle of 90 degrees. The edges of the sector along the radius are meshed with N_r cells, whereas the third side is meshed with $\frac{3}{2}N_r$ cells. A sequence of meshes with $N_r=50$, 100, 200 is considered. In order to test the performance of our methods an artificially poor mixed element mesh is deliberately constructed as follows. Inside the computational domain a quadrilateral subdomain $0.5\leq x\leq 0.8$, $-0.25\leq y\leq 0.25$ is selected and meshed it using the quadrilateral elements. The rest of the domain is
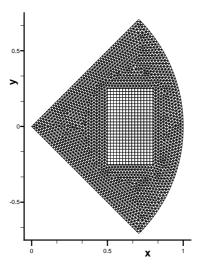
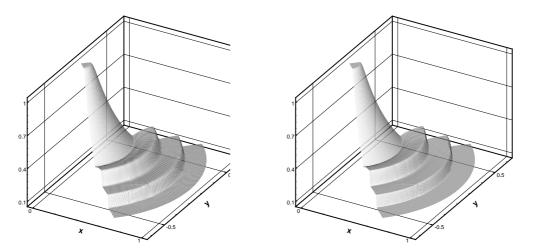Figure 8: A mixed-element mesh with $N_r = 50$ for the cylindrical explosion problem (5.2).

Figure 9: Density plots for WENO-3 scheme for $N = 100$ (left) and $N = 200$ (right) meshes for the cylindrical explosion problem (5.2).

discretized using triangles. Fig. 8 illustrates the resulting mixed-element mesh for $N_r = 50$, which corresponds to the total number of 3874 computational cells. The discontinuity in the initial data crosses the interface between quadrilateral and triangular cells thus making this mesh a very good setup to test the sensitivity of the scheme.

The numerical solution is computed at output time $t = 0.25$ using the WENO-3 scheme. The results of the two-dimensional run are compared with a reference radial solution by solving numerically the one-dimensional Euler equations with a geometrical source term. Fig. 9 shows the contour plots of density on mixed-element meshes with $N = 100$ and $N = 200$. Fig. 10 shows a comparison between the one-dimensional reference ra-
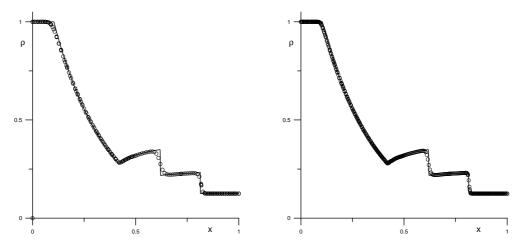
Figure 10: WENO-3 results for $N_r = 100$ (left) and $N_r = 200$ (right) for the cylindrical explosion problem (5.2).

dial solution (solid line) and the cell averages of the two-dimensional WENO-3 solution (symbols) along the radial line that is coincident with the x-axis. The distributions of gas density ρ for $x > 0$ are presented. The solution contains a cylindrical shock wave and a contact surface traveling away from the centre and a rarefaction wave traveling towards the origin (0,0,0). It is observed that the scheme produces the correct flow pattern with the correct values behind the shock wave and the contact surface. The slight artifacts at the interface between quadrilateral and triangular cells in the surface plots are most probably produced by the post-processing software.

Similar conclusions have been drawn for the WENO-5 scheme. The results are omitted.

5.2 A Mach-3 wind tunnel with a step

This problem is from [24]. The compressible Euler equations (4.1) are solved in a wind tunnel 3 lengths units long and 1 length unit wide. The step is 0.2 length units high and is located 0.6 length units from the left of the tunnel. The flow is initialized with a right-going flow of Mach number equal to 3. Reflective boundary conditions are applied along the walls of the tunnel, and inflow and outflow boundary conditions are used at the entrance and the exit. The corner step is a singularity point and on Cartesian meshes special techniques can be used to treat it [24]. No such treatment is used in the present work.

For this problem a mixed-element mesh with a boundary layer is constructed as follows. The left, right, top and bottom ($0 < x < 0.6$, $y = 0$) boundaries of the computational domain are divided into uniform intervals with the size $h = 1/N$, $N = 40, 80, 160$. The other two boundary parts, corresponding to the step, are discretised using mesh stretching to the corner point so that the boundary cell size grows from $h/5$ to h. Next, a boundary layer is attached to the step walls and the rest of the domain is meshed using triangular
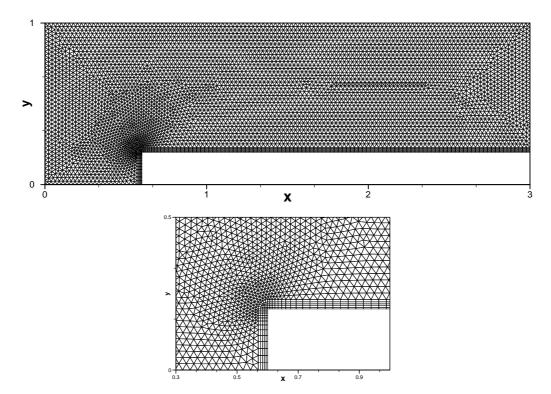
Figure 11: Mixed-element mesh for the Mach-3 wind tunnel problem.

cells. Fig. 11 shows the general view of the mesh in the case $N=40$ including the details of the region near the corner of the step. Due to the presence of the boundary layer and a transition from the quadrilateral cells to triangular ones near the corner of the step, where intensive wave interaction takes place, the Mach-3 wind tunnel flow with this particular mesh is a suitable test problem to verify the performance and robustness of the methods as applied to shock-dominated flows with solid boundaries.

Fig. 12 shows the results of the convergence studies using the third-order scheme. A sequence of three meshes corresponding to $N=40$, 80 and 160 is considered. Comparing these results to those in the existing literature [10, 24] it is concluded that the WENO-3 method produces the flow pattern generally accepted at present as correct, on all meshes; shock waves and contact discontinuities are well resolved and correctly positioned.

6   Conclusions

In this paper an extension of the existing finite-volume WENO schemes to mixed-element unstructured meshes in two space dimensions was presented. The new schemes have been applied to a number of well-established test problems with both smooth and discontinuous solutions.
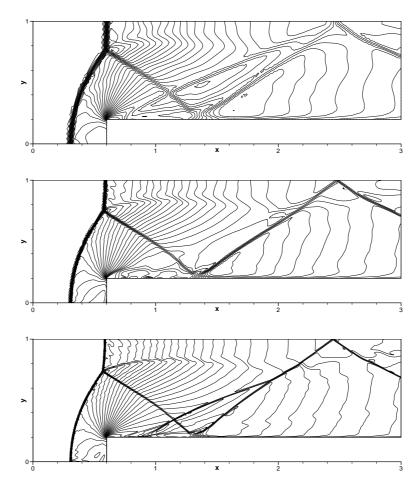
Figure 12: Density for the Mach-3 wind tunnel problem on the $N=40$ (top), 80 (middle) and 160 (top) meshes. Thirty contour from 0.12 to 6.41.

The presented numerical results demonstrate that:

- The schemes achieve the designed order of accuracy for both triangular and quadri-lateral meshes.

- For mixed-element meshes the very high order of spatial accuracy IS maintained across interfaces between cells of two different types.

- The performance of the schemes is only mildly affected by the quality of the mesh.

- For discontinuous solutions there are little, if any, numerical artifacts at interfaces between neighbouring cells of two different types.

The future developments will include extensions to the three-dimensional case and to the ADER approach [3, 4, 16, 20, 22, 23], as well as application to Large Eddy Simulations of unsteady turbulent flows [8, 17].

References

[1] D.S. Balsara and C.-W. Shu. Monotonicity preserving weighted essentially non-oscillatory schemes with increasingly high order of accuracy. J. Comput. Phys., 160:405–452, 2000.

[2] T.J. Barth and P.O. Frederickson. Higher order solution of the Euler equations on unstructured grids using quadratic reconstruction. In AIAA paper no. 90-0013, 28th Aerospace Sciences Meeting, 1990.

[3] M. Dumbser and M. Käser. Arbitrary high order non-oscillatory finite volume schemes on unstructured meshes for linear hyperbolic systems. Journal of Computational Physics, 221(2):693–723, 2007.

[4] M. Dumbser, M. Käser, V.A. Titarev, and E.F. Toro. Quadrature-free non-oscillatory finite volume schemes on unstructured meshes for nonlinear hyperbolic systems. Journal of Computational Physics, 226:204–243, 2007.

[5] G.E. Forsythe, M.A. Malcolm, and C.B. Moler. Computer Methods for Mathematical Computations. Englewood Cliffs, NJ: Prentice-Hall, 1977.

[6] O. Friedrichs. Weighted essentially non-oscillatory schemes for the interpolation of mean values on unstructured grids. Journal of Computational Physics, 144(1):194–212, 1998.

[7] S.K. Godunov. A finite difference method for the computation of discontinuous solutions of the equations of fluid dynamics. Mat. Sbornik, 47:357–393, 1959.

[8] M. Hahn and D. Drikakis. Assessment of large-eddy simulation of internal separated flow. Journal of Fluids Engineering, 131(7):071201, 2009.

[9] A. Harten, P.D. Lax, and B. van Leer. On upstream differencing and Godunov-type schemes for hyperbolic conservation laws. SIAM Review, 25(1):35–61, 1983.

[10] C. Hu and C.-W. Shu. Weighted essentially non-oscillatory schemes on triangular meshes. J. Comput. Phys., 150:97–127, 1999.

[11] G.S. Jiang and C.W. Shu. Efficient implementation of weighted ENO schemes. J. Comput. Phys., 126:202–212, 1996.

[12] M. Käser and A. Iske. ADER schemes on adaptive triangular meshes for scalar conservation laws. J. Comput. Phys., 205:486–508, 2005.

[13] A.G. Kulikovskii, N.V. Pogorelov, and A.Yu. Semenov. Mathematical Aspects of Numerical Solution of Hyperbolic Systems. Chapman and Hall, 2002. Monographs and Surveys in Pure and Applied Mathematics, Vol. 118.

[14] X.D. Liu, S. Osher, and T. Chan. Weighted essentially non-oscillatory schemes. J. Comput. Phys., 115:200–212, 1994.

[15] A.H. Stroud. Approximate calculation of multiple integrals. Prentice-Hall Inc., Englewood Cliffs, NJ, 1971.

[16] A. Taube, M. Dumbser, D.S. Balsara, and C.-D. Munz. Arbitrary High-Order Discontinuous Galerkin Schemes for the Magnetohydrodynamic Equations. Journal of Scientific Computing, 30(3):441–464, 2007.

[17] B. Thornber, A. Mosedale, and D. Drikakis. On the implicit large eddy simulations of homogeneous decaying turbulence. Journal of Computational Physics, 226:1902–1929, 2007.

[18] V.A. Titarev, E.I. Romenski, and E.F. Toro. MUSTA-type upwind fluxes for non-linear elasticity. Int. J. Num. Methods in Eng., 73:897–926, 2008.

[19] V.A. Titarev and E.F. Toro. Finite-volume WENO schemes for three-dimensional conservation laws. J. Comput. Phys., 201(1):238–260, 2004.

[20] V.A. Titarev and E.F. Toro. ADER schemes for three-dimensional nonlinear hyperbolic systems. J. Comput. Phys., 204(2):715–736, 2005.

[21] E.F. Toro. Riemann Solvers and Numerical Methods for Fluid Dynamics. Springer-Verlag, third edition, 2009.

[22] E.F. Toro, R.C. Millington, and L.A.M. Nejad. Towards very high order Godunov schemes. In E.F. Toro, editor, Godunov Methods. Theory and Applications, pages 907–940. Kluwer/Plenum Academic Publishers, 2001.

[23] E.F. Toro and V.A. Titarev. Solution of the generalised Riemann problem for advection-reaction equations. Proc. Roy. Soc. London, 458 (2018):271–281, 2002.

[24] P. Woodward and P. Colella. The numerical simulation of two-dimensional fluid flow with strong shocks. J. Comput. Phys., 54:115–173, 1984.

[25] Y.-T. Zhang and C.-W. Shu. Third order WENO scheme on three dimensional tetrahedral meshes. Communications in Computational Physics, 5(2-4):836–848, 2009.